Supplementary Information (SI) for Green Chemistry.
This journal is © The Royal Society of Chemistry 2025

Electronic Supplementary Material (ESI) for Green Chemistry

Enhancing catalytic performance of intergrowth ferroelectric $Bi_5TiNbWO_{15}$ through strong synergistic photo-tribo-piezo multi-field polarization

*Hongjian Yu[a, *], Xiaole Li[a], Rufang Zhao[b], Keyang Wang[c, d], Yuxuan Liao[a], Chendi Shi[a], Shuchen Tu[e], Hiang Kwee Lee[f, *], Fan Guo[a], Jie Han[a, *]*

[a] China Jiangsu Provincial Key Laboratory of Green & Functional Materials and Environmental Chemistry, College of Chemistry and Chemical Engineering, Yangzhou University, Yangzhou 225002, China

[b] Hubei Key Laboratory of Pollutant Analysis & Reuse Technology, College of Chemistry and Chemical Engineering, Hubei Normal University, Huangshi 435002, China

[c]The Aviation Technician NCO School, Air Force Engineering University. Xinyang, 464000, China

[d]College of civil engineering and mechanics, Lanzhou University, Lanzhou, Gansu, P.R. China.

[e]SCNU Environmental Research Institute, Guangdong Provincial Key Laboratory of Chemical Pollution and Environmental Safety & MOE Key Laboratory of Theoretical Chemistry of Environment, School of Environment, South China Normal University, Guangzhou, 510006, China

[f]Division of Chemistry and Biological Chemistry, School of Chemistry, Chemical Engineering and Biotechnology, Nanyang Technological University, 21 Nanyang Link, 637371, Singapore.

[*] Corresponding authors: yhj@yzu.edu.cn; hiangkwee@ntu.edu.sg; hanjie@yzu.edu.cn

1. Experimental section

1.1. Chemicals

Bismuth trioxide (Bi_2O_3), titanium dioxide (TiO_2), potassium iodide(KI), EDTA-2Na, and 5,5-dimethyl-1-pyrroline N-oxide (DMPO) were purchased from Shanghai Aladdin Biochemical Technology Co., Ltd. Tungsten trioxide (WO_3), isopropanol (IPA), rhodamine B (RhB, $C_{28}H_{31}ClN_2O_3$), methylene blue (MB, $C_{16}H_{18}N_3ClS$), ammonium molybdate tetrahydrate ($H_{24}Mo_7N_6O_{24}\cdot 4H_2O$), tetracycline hydrochloride (TC, $C_{22}H_{25}ClN_2O_8$), and ciprofloxacin (CIP, $C_{17}H_{18}FN_3O_3$) were purchased from Shanghai Macklin Biochemical Co., Ltd. Niobium oxide (Nb_2O_5) and L (+)-ascorbic acid (LAA) were purchased from Sinopharm Chemical Reagent Co., Ltd.

1.2. Preparation of Bi_2WO_6 (BWO)

The BWO was prepared by conventional solid-state reaction method. The raw materials Bi_2O_3 and WO_3 were mixed evenly according to the stoichiometric ratio and ball milled for 12 h with anhydrous ethanol as a ball-milling medium. The mixture was then dried and sintered at 850 ^oC for 7 h in the muffle furnace. Finally, the as-prepared product was ground into powders and collected for further analysis.

1.3. Preparation of Bi_3TiNbO_9 (BTNO)

The BTNO was prepared by conventional solid-state reaction method. The raw materials Bi_2O_3, TiO_2, and Nb_2O_5 were mixed evenly according to the stoichiometric ratio and ball milled for 12 h with anhydrous ethanol as a ball-milling medium. The mixture was dried and sintered at 1000 ℃ for 4 h in the muffle furnace. Finally, the as-prepared product was ground into powders and collected for further analysis.

1.4. Preparation of $Bi_5TiNbWO_{15}$ (BTNWO)

The BTNWO was prepared by conventional solid-state reaction method. The raw materials Bi_2O_3, TiO_2, Nb_2O_5, and WO_3 were mixed evenly according to the stoichiometric ratio and ball milled for 12 h with anhydrous ethanol as a ball-milling medium. The mxiture was then dried and pre-sintered at 850 ℃ for 7 h in the muffle furnace. Subsequently, the pre-sintered product was ball milled for 12 h again and sintered at 1000 ℃ for 4 h. Finally, the as-prepared product was ground into powders and collected for further analysis.

1.5. Characterization

The phases of as-prepared samples were analyzed using an X-ray diffractometer (D8 Advance, Bruker AXS) with Cu Kα radiation (λ =1.5418 Å). The morphology, nano-micro-structures, and elemental composition of prepared samples were observed on a field emission scanning electron microscopy (GeminiSEM 300, ZEISS) and a high-resolution transmission electron microscopy (Tecnai G2 F30 S-Twin TEM, FEI). Specific surface areas were measured by the nitrogen adsorption-desorption using a Brunauer-Emmett-Teller (BET) analysis instrument (Beishide 3H-2000PS2). The chemical compositions of samples were assessed by X-ray photoelectron spectroscopy (ESCALAB 250 spectrometer, Thermo Scientific). UV-vis diffuse reflectance spectra (DRS) were measured on a UV-Vis-NIR spectrophotometer (Cary 5000 Varian, Agilent) and white $BaSO_4$ was used as reference. Electron paramagnetic resonance (EPR) measurement was taken on a Bruker spectrometer (A300-10/12, Bruker). High-performance liquid chromatography-mass spectrometer (HPLC-MS, waters2695-

ZQ2000) was used to analyze the main intermediate products of Rhodamine B degradation process. Amplitude, phase mapping, butterfly curves, and phase hysteresis loops were measured by piezoresponse force microscopy module (PFM), and the surface potential of samples were monitored by Kelvin probe force microscopy (KPFM) in atomic force microscopy (MFP-3D, Oxford). The active free radical signals were recorded by an electron spin resonance (ESR) spectrometer (EMXPLUS, Bruker). Finite element method (FEM) using COMSOL Multiphysics software was used to simulate the piezoelectric potentials of all samples under 100 MPa pressure. The open-circuit voltage was measured by high impedance electrometer (Keithley 6514).

1.6. Photocatalytic degradation test

Photocatalytic degradation experiments were measured in a 250 mL custom three-necked quartz flask reactor with a cooling water cycle to keep the reaction temperature of the aqueous solution at 25 ± 5 °C. 50 mg catalyst was first dispersed into 100 mL of aqueous Rhodamine B solution (RhB, 5 mg/L). Prior to light irradiation, the suspensions were stirred at a rate of 100 rpm for 30 min in dark to achieve an adsorption-desorption equilibrium between the catalyst and RhB. The photocatalysis was then initiaited under light illumination (300 W Xe lamp with an AM1.5 G filter, 20 cm between the lamp and specimen, irradience of 100 mW/cm^2, irradiation area of 12.6 cm^2). 3 mL aliquot of RhB solution was extracted at 15 min intervals and centrifuged to remove the catalyst. Finally, the concentration of RhB was analyzed by recording the peak absorbance recorded using the UV-vis absorption spectra (Mapada UV-6100).

1.7. Tribocatalytic activity measurements

The tribocatalytic behavior of catalysts was estimated by using a model reaction involving RhB degradation under stirring and dark conditions with temperature maintained at 25 ± 5 °C. Firstly, 50 mg catalyst was dispersed into 100 mL of contaminant Rhodamine B (RhB, 5 mg/L) in a 250 mL custom-made three-necked quartz flask reactor. The suspensions were stirred for 30 min at a rate of 100 rpm in the dark with the stirring paddle (polytetrafluoroethylene, PTFE) to ensure adsorption equilibrium. The suspension was then stirred at an increased rate of 600 rpm with the stirring paddle at the bottom of a three-necked flask. During the tribo-catalytic process, 3 mL suspension was collected at every 2 h interval and immediately centrifuged to remove catalyst. Finally, the concentration of RhB was analyzed by recording the peak absorbance in the UV-vis absorption spectra (Mapada UV-6100).

1.8. Piezocatalytic degradation tests

Piezocatalytic degradation of pollutants was performed in an ultrasonic cleaner (KQ-400DE, 40 kHz, 240 W, Kunshan Ultrasonic Instruments Co., Ltd) with an electric stirrer at 25 ± 5 °C under dark conditions. Typically, 50 mg of catalysts powder was dispersed in 100 mL of RhB (100 mg/L) solution in a 250 mL custom-made three-necked quartz flask reactor. Then, the above suspension was stirred at a low stirring speed of 100 rpm for 30 min to reach the adsorption-desorption equilibrium between catalysts and RhB. Subsequently, the three-necked quartz flask reactor was placed into the ultrasonic cleaner and the ultrasonicator was turned on with the reaction solution stirring at 100 rpm. During the 60 min of degradation process, 3 mL aliquots of RhB

solution was extracted every 15 min and immediately centrifuged to remove catalyst. Finally, the concentration of RhB was analyzed by recording the peak absorbance in the UV-vis absorbance spectra (Mapada UV-6100).

1.9. Photo-piezocatalytic, tribo-piezocatalytic and photo-tribo-piezocatalytic degradation tests

Photo-piezocatalytic, tribo-piezocatalytic, and photo-tribo-piezocatalytic degradation experiments were performed according to various combinations of the above-mentioned experimental protocols. The concentration of rhodamine B (RhB), methylene blue (MB), tetracycline hydrochloride (TC), and ciprofloxacin (CIP) used for the experiments were 100, 10, 10, and 5 mg/L, respectively.

1.10. Photo-tribo-piezocatalytic H_2O_2 generation tests

50 mg of catalyst powder was dispersed in 50 ml of deionized water in a 250 mL custom three-necked quartz flask reactor. Photo-tribo-piezocatalytic H_2O_2 generation experiments employed the same experimental setup as photo-tribo-piezocatalytic degradation experiments. The concentration of H_2O_2 was determined by iodometry. Specifically, 500 μL aliquot of the solution was extracted every 15 min after high-speed centrifugation. 50 μL of 0.01 M ammonium molybdate solution and 2 mL of 0.1 M potassium iodide (KI) solution were then added and allowed to react for 15 min. The maximum absorbance intensity of the resultant solution at 352 nm was recorded using a UV-6100 spectrophotometer.

1.11. Calculation of specific energy consumption (SEC)

The SEC was calculated based on the total electrical energy consumed by the active energy-input devices, including Xe lamp, ultrasonic cleaner, mechanical stirrer,

and other devices during the reaction time, which was then divided by the mass of product generated (i.e., H_2O_2 produced or RhB degraded). The rated power (as shown in Tables S1 and S2) corresponds to the nominal electrical input power of these devices, or to values measured under actual operating conditions using a calibrated power meter according to the literature. The specific energy consumption for H_2O_2 production and RhB degradation is calculated according to the following equation:

$$SEC = \frac{Pt}{m}$$

where P denotes the total power of the electrical input devices during the catalytic reaction, t denotes the duration of the catalytic reaction, and m represents the mass of H_2O_2 production or the mass of RhB degradation.

1.12. Electrochemical test

Piezo-current response, Mott-Schottky, and electrochemical impedance spectroscopy (EIS) measurements were carried out using an electrochemical workststion (CHI-760E, Chenhua Instruments Co., Ltd) with a standard three-electrode system. The samples, saturated calomel electrode (SCE), and platinum (Pt) wire were used as the working electrode, the reference electrode, and the counter electrode, respectively. 0.1 M aqueous Na_2SO_4 solution was used as the electrolyte. The mechanical agitation was generated by an ultrasonic cleaner (KQ-400DE 40 kHz, 240 W, Kunshan Ultrasonic Instruments Co., Ltd) during the measurement process. 10 mg sample powder was deposited onto the surface of ITO glass substrate (2 cm × 4 cm) using conductive adhesive.

1.12. Density functional theory (DFT) calculation

This study employed first-principles calculations based on density functional

theory (DFT) with periodic boundary conditions. All calculations were performed using the Vienna Ab initio Simulation Package (VASP 5.4.4).[1,2] The exchange-correlation potential was described using the Perdew-Burke-Ernzerhof (PBE) functional within the generalized gradient approximation (GGA).[3] To mitigate the self-interaction error inherent in DFT, the GGA + U method was adopted for an accurate treatment of the d-electrons of transition metals, with the Hubbard U parameters for Ti 3d and Nb 4d orbitals both set to 4 eV. The electronic wave functions were expanded in a plane-wave basis set with a cutoff energy of 450 eV to ensure computational convergence. The interaction between core and valence electrons was approximated using the Projector Augmented-Wave (PAW) method.[4,5] Furthermore, van der Waals corrections were incorporated using the DFT-D3 method with Becke-Johnson damping to accurately describe the weak interlayer interactions.[6]

To investigate the band gap and projected density of states (PDOS) in the symbiotic layered structure, simulations were conducted based on a bulk-structured model. This model consisted of 2 Ti layers, 10 Bi layers, 2 Nb layers, and 2 W layers, comprising a total of 92 atoms, with lattice parameters of a = 5.42310 Å, b = 5.40270 Å, and c = 42.74400 Å (Fig. S38). A 5 × 5 × 1 k-point mesh was employed to sample the Brillouin zone. Additionally, the bulk phase structure and the model used for simulating O_2 adsorption on the BW-BTN (001) perovskite-like surface were depicted in Fig. S39 and Fig. S40, with the Brillouin zone sampled using a 2 × 2 × 1 k-point mesh. During geometry optimization, all atoms were allowed to relax until the total energy reduction fell below a convergence threshold of 1×10^{-5} eV. Furthermore, the atomic forces were

constrained to be less than 0.03 eV/Å to ensure proper atomic position optimization. To eliminate artificial interactions between periodic images along the z-direction, a vacuum layer of 15 Å was introduced in all slab models.

To evaluate the adsorption strength of O_2 molecules on the BT-BTN (001) surface, the adsorption energy (E_{ads}) is defined as:

$$E_{ads}^{O_2} = E(O_2 + BTNWO\ (001)) - E(BTNWO\ (001)) - E(O_2) \quad (1)$$

where *E(O_2 + BTNWO (001))* represents the total energy of the combined system when an O_2 molecule is adsorbed on the BTNWO (001) surface, *E(BTNWO (001))* denotes the energy of the pristine BTNWO (001) surface, and *E(O_2)* corresponds to the energy of an isolated O_2 molecule in vacuum. A more negative adsorption energy indicates higher thermodynamic stability of the adsorption structure.

2. Supplementary Figures

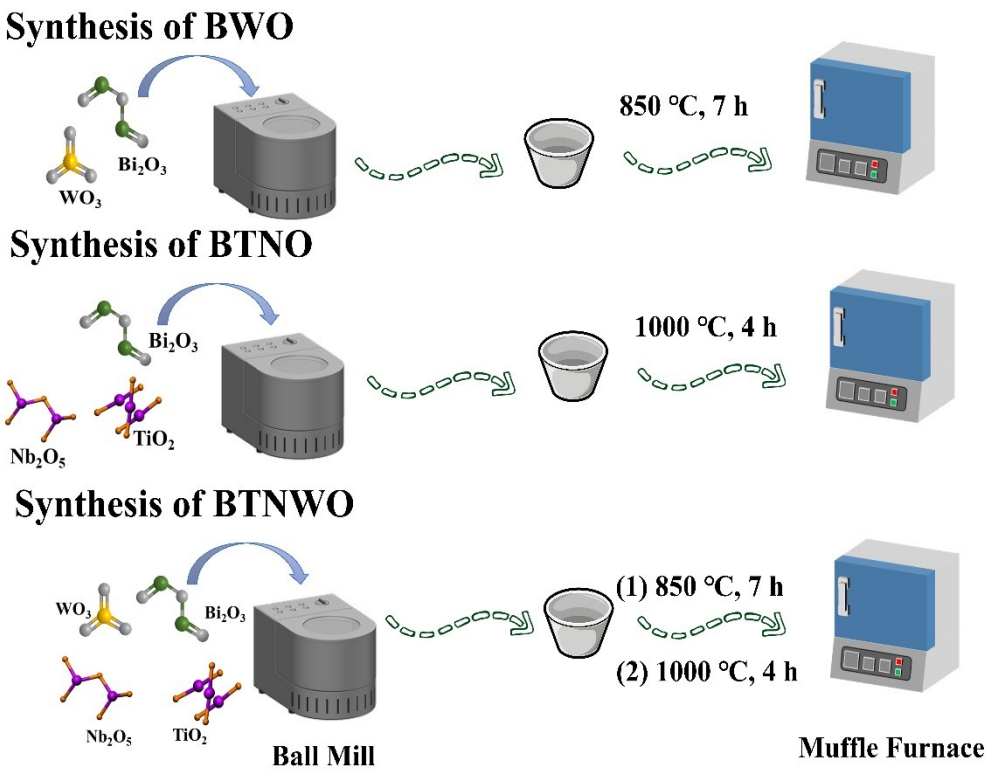

Fig. S1. Scheme illustrating the fabrication process of various samples.

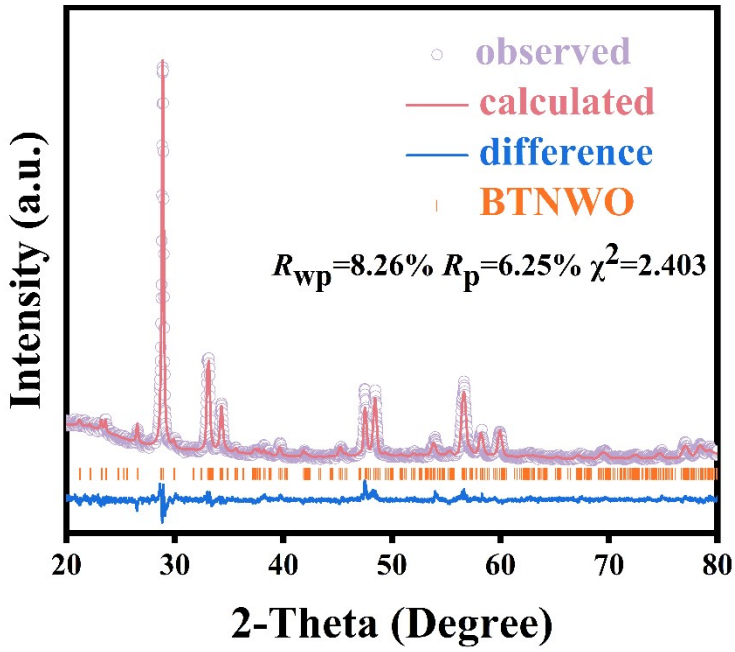

Fig. S2. Rietveld refinement of the XRD pattern of BTNWO.

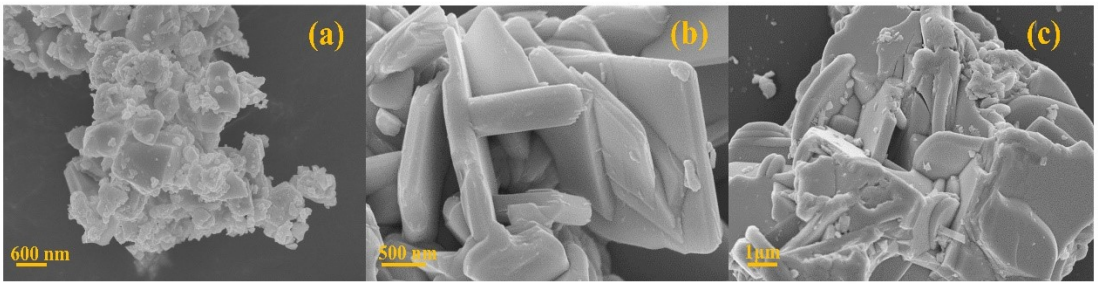

Fig. S3. SEM images of as-prepared (a) BWO, (b) BTNO, and (c) BTNWO.

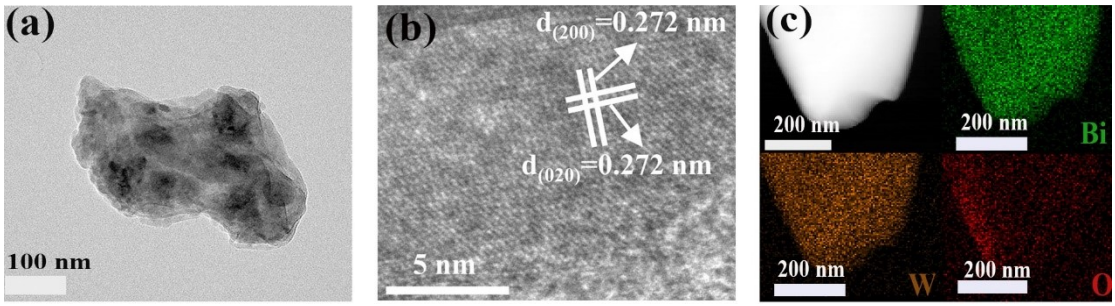

Fig. S4. (a) TEM image, (b) HRTEM image, and (c) EDX elemental mappings of Bi, W, and O elements on BWO.

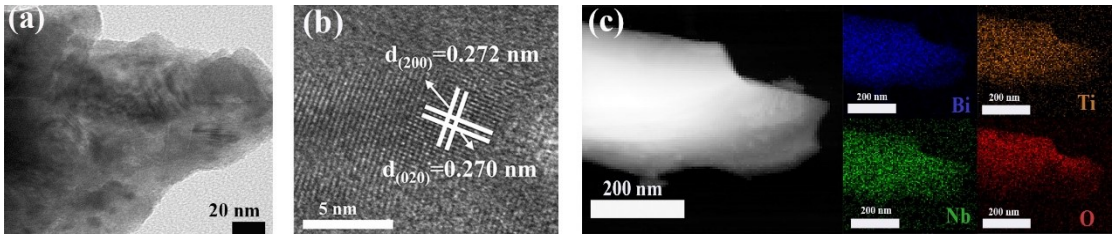

Fig. S5. (a) TEM image, (b) HRTEM image, and (c) elemental mappings of Bi, Ti, Nb, and O elements on BTNO.

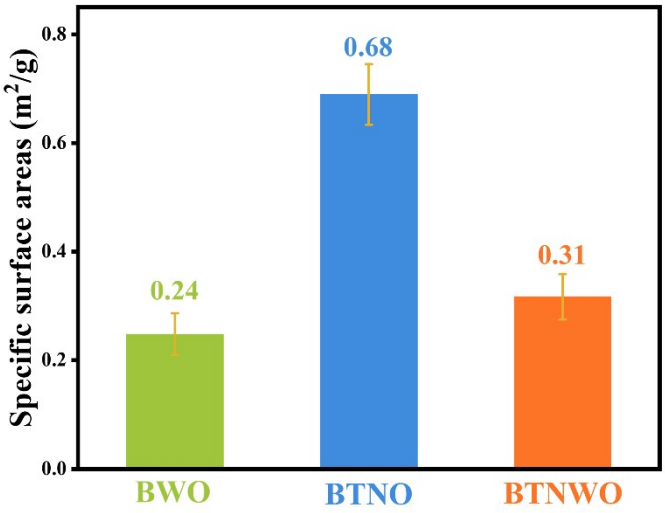

Fig. S6. Specific surface areas of BWO, BTNO, and BTNWO.

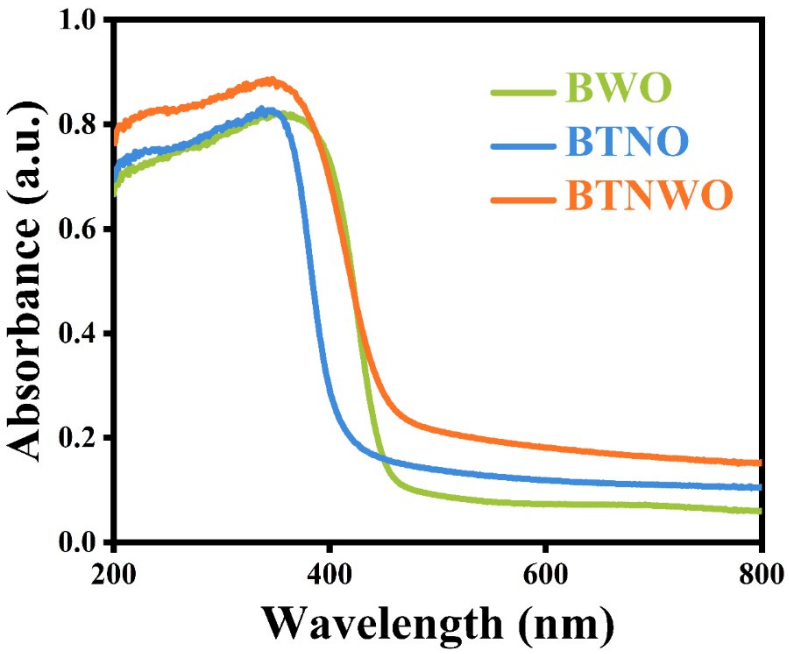

Fig. S7. UV-vis diffuse reflectance spectra of BWO, BTNO, and BTNWO.

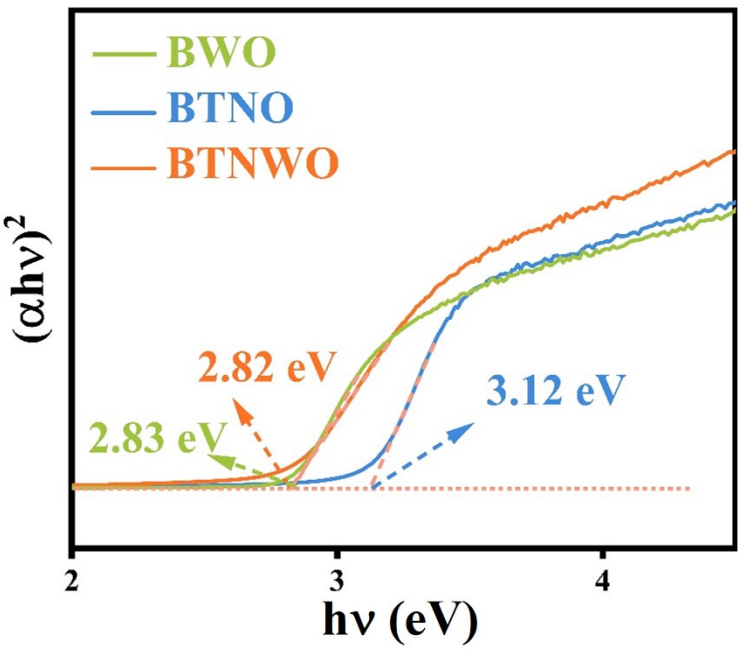

Fig. S8. Tauc plots showing the band gap values of BWO, BTNO, and BTNWO.

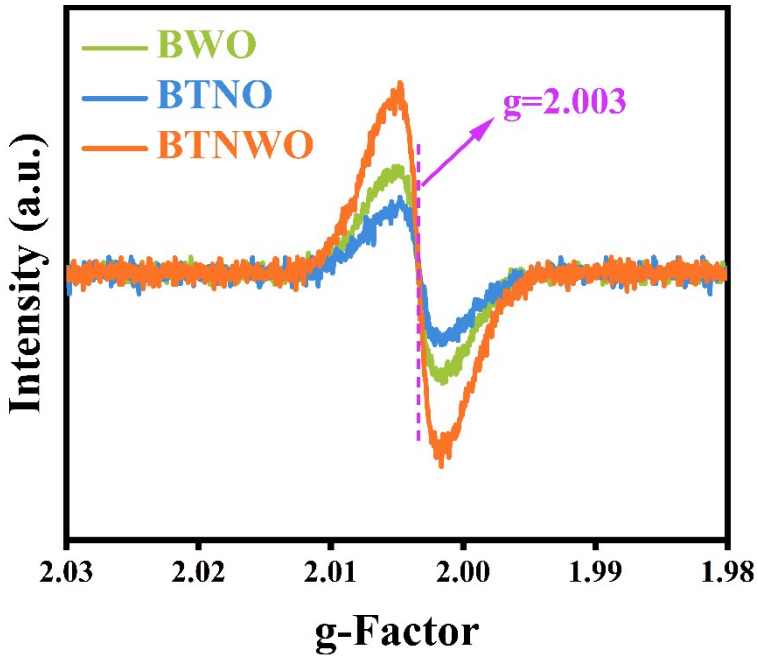

Fig. S9. EPR spectra of BWO, BTNO, and BTNWO.

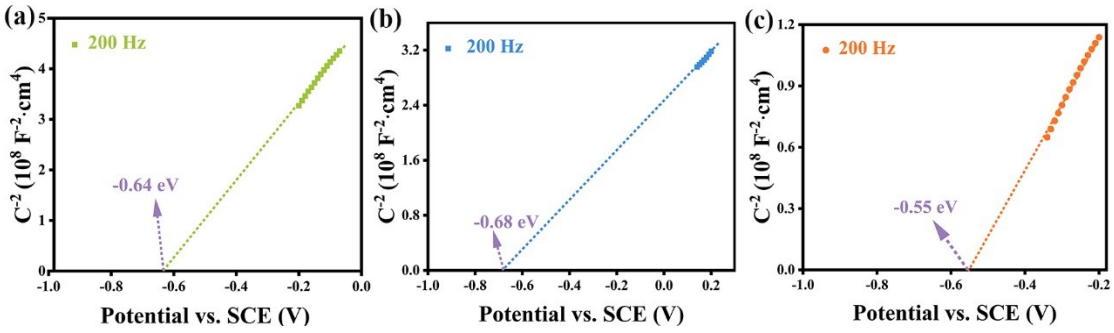

Fig. S10. Mott-Schottky plots of (a) BWO, (b) BTNO, and (c) BTNWO (0.1 M Na_2SO_4).

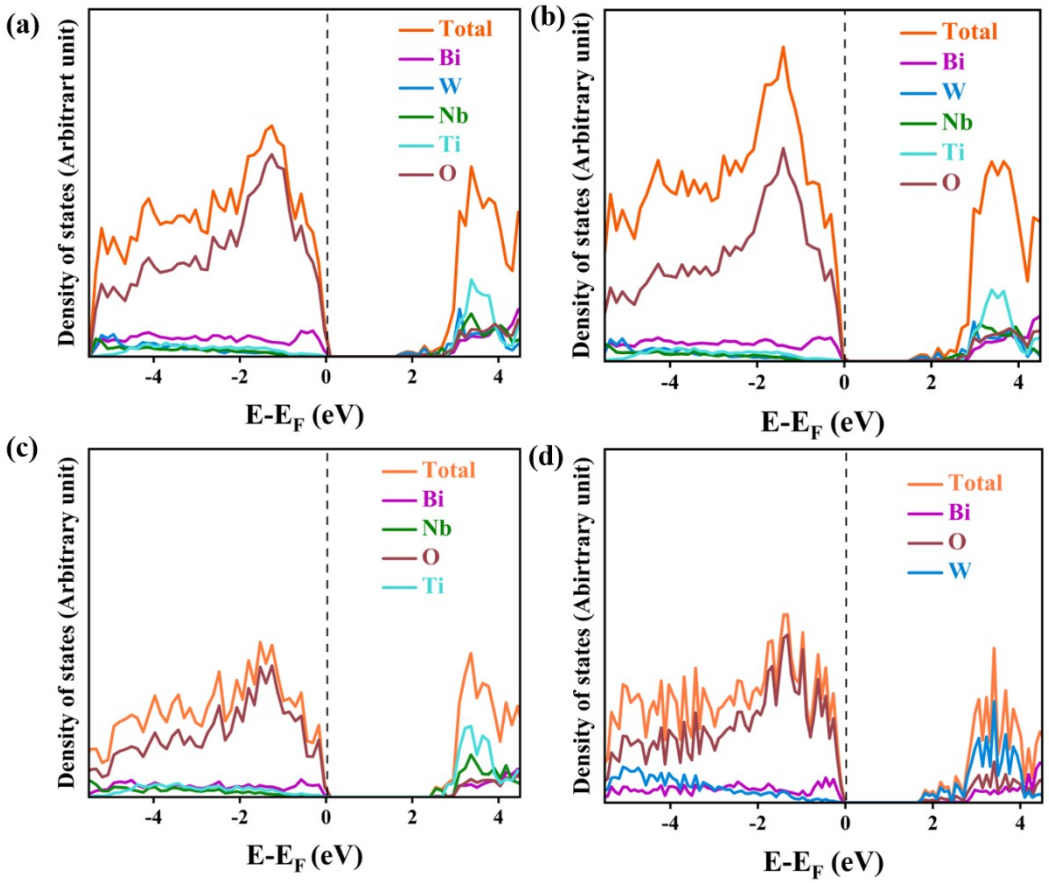

Fig. S11. (a, b) DOS and PDOS of BTNWO and BTNWO under stress. (c, d) DOS and PDOS of BTNO and BWO.

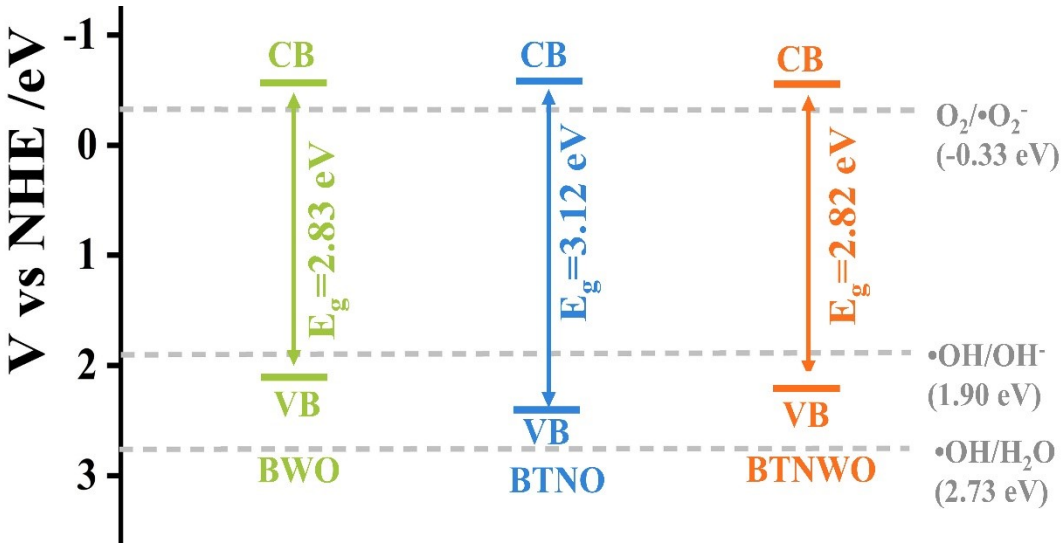

Fig. S12. The energy band structure diagrams of BWO, BTNO, and BTNWO.

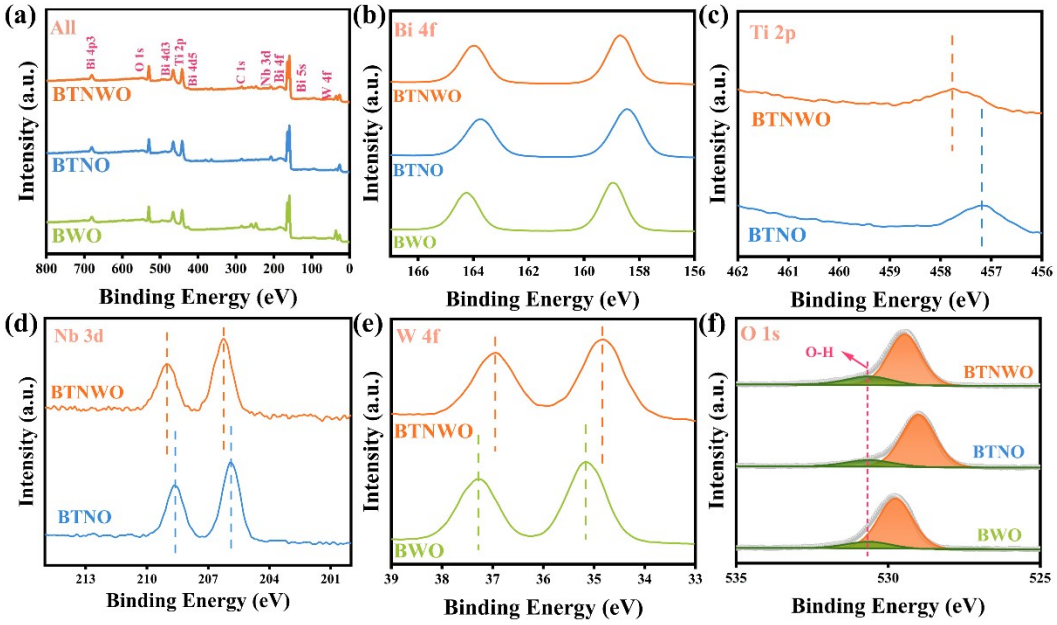

Fig. S13. XPS spectra of (a) survey, (b) Bi 4f, (c) Ti 2p, (d) Nb 3d, (e)W 4f, and (f) O 1s of BWO, BTNO, and BTNWO.

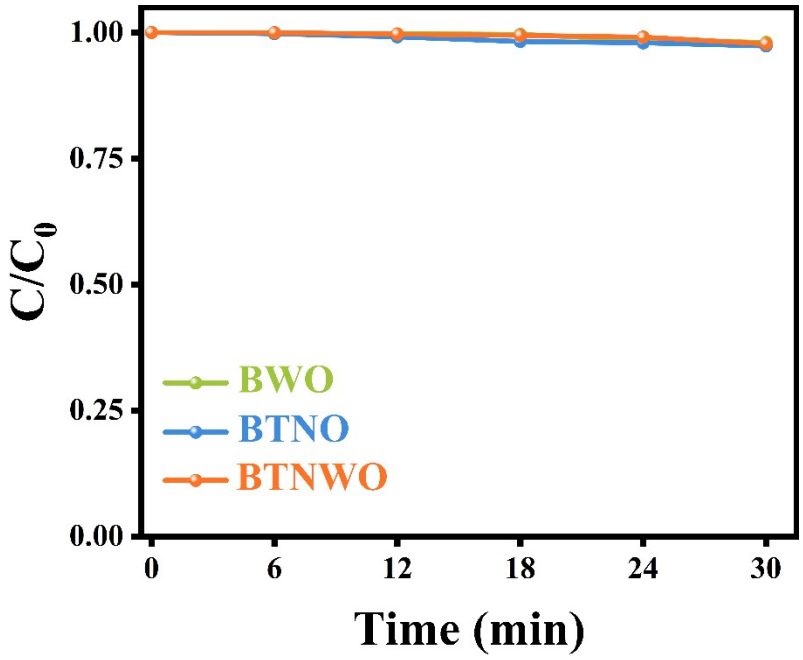

Fig. S14. Time-dependent change in pollutant concentration arising from adsorption on BWO, BTNO, and BTNWO under dark conditions.

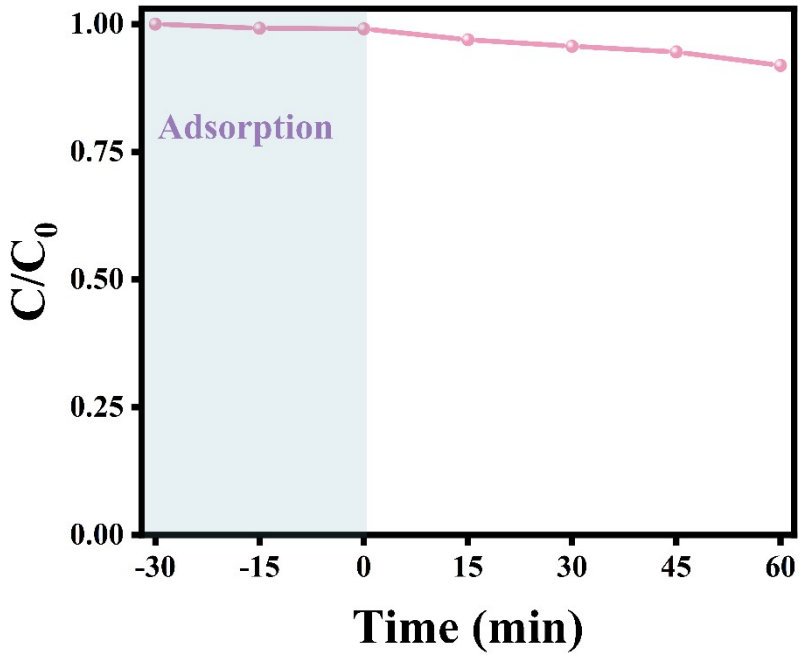

Fig. S15. Adsorption (under dark conditons) and degradation of RhB (100 mg/L) in the catalyst-free system under concurrent irradiation, friction stirring, and ultrasonic vibration.

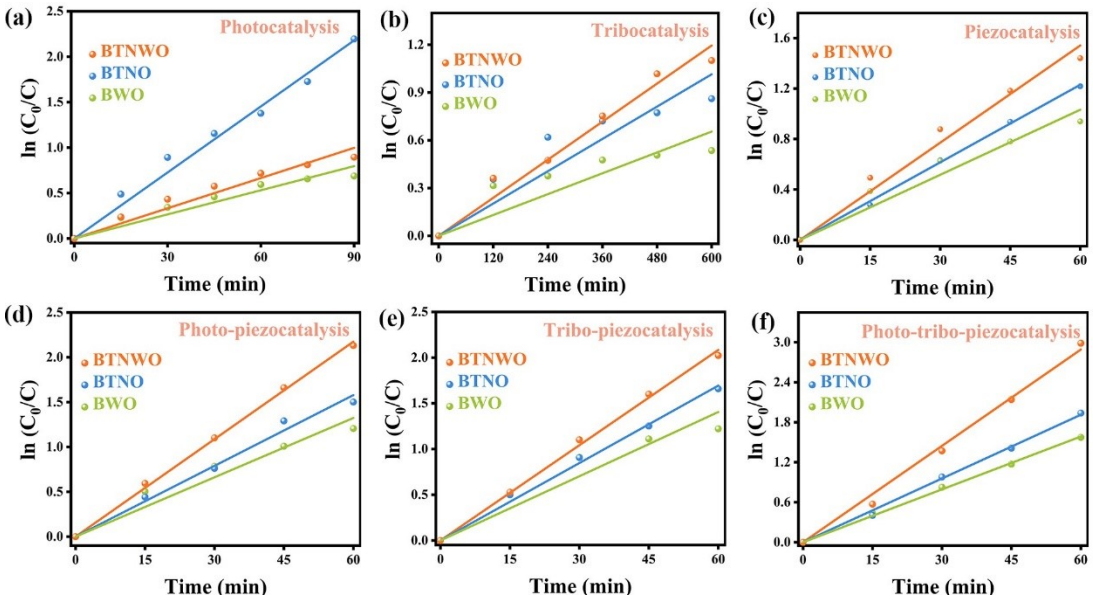

Fig. S16. ln (C_0/C)-t curves of all samples during (a) photocatalysis, (b) tribocatalysis, (c) piezocatalysis, (d) photo-piezocatalysis, (e) tribo-piezocatalysis, and (f) photo-tribo-piezocatalysis.

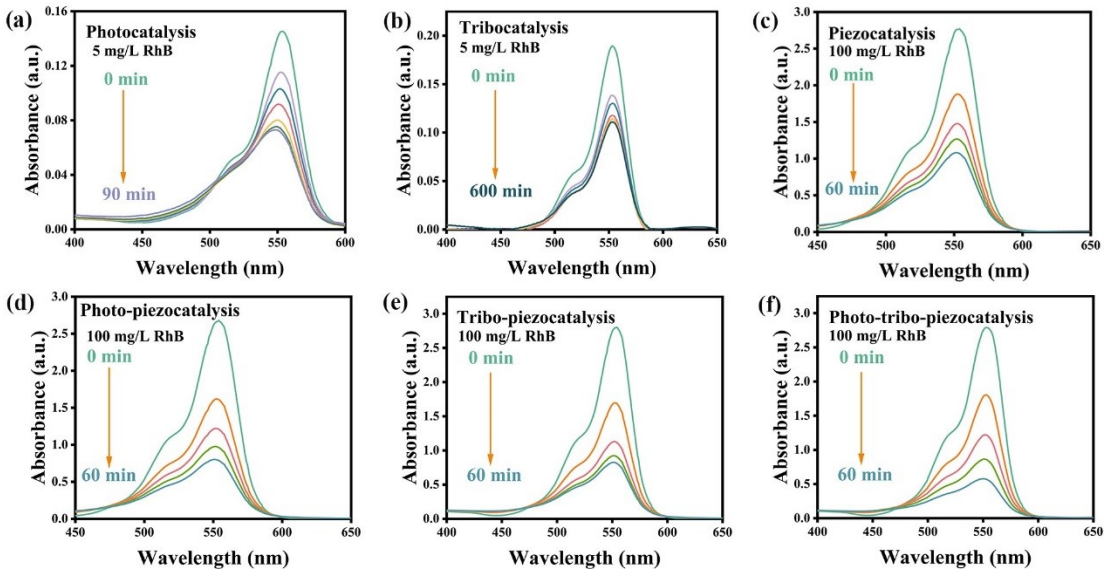

Fig. S17. Time-dependent UV-vis absorption spectra of reaction solution during (a) photocatalytic, (b) tribocatalytic, (c) piezocatalytic, (d) photo-piezocatalytic, (e) tribo-piezocatalytic, and (f) photo-tribo-piezocatalytic RhB degradations by BWO.

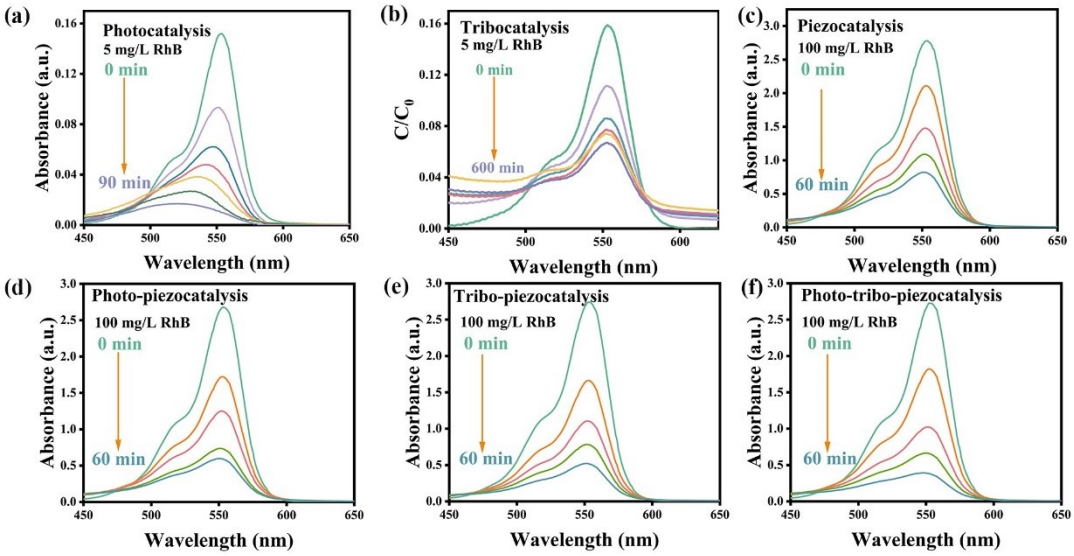

Fig. S18 Time-dependent UV-vis absorption spectra of reaction solution during (a) photocatalytic, (b) tribocatalytic, (c) piezocatalytic, (d) photo-piezocatalytic, (e) tribo-piezocatalytic, and (f) photo-tribo-piezocatalytic RhB degradations by BTNO.

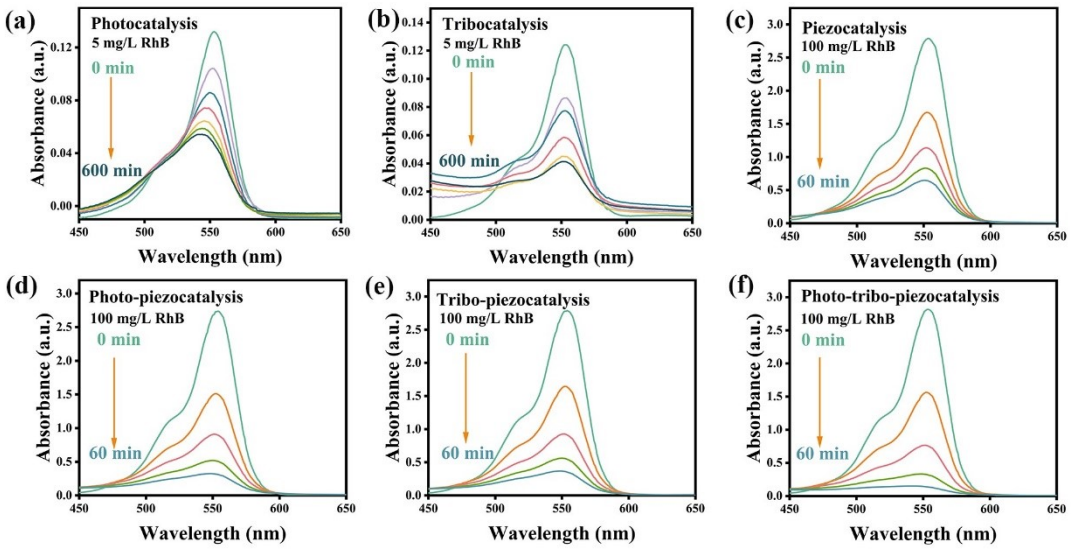

Fig. S19. Time-dependent UV-vis absorption spectra of reaction solution during (a) photocatalytic, (b) tribocatalytic, (c) piezocatalytic, (d) photo-piezocatalytic, (e) tribo-piezocatalytic, and (f) photo-tribo-piezocatalytic RhB degradations by BTNWO.

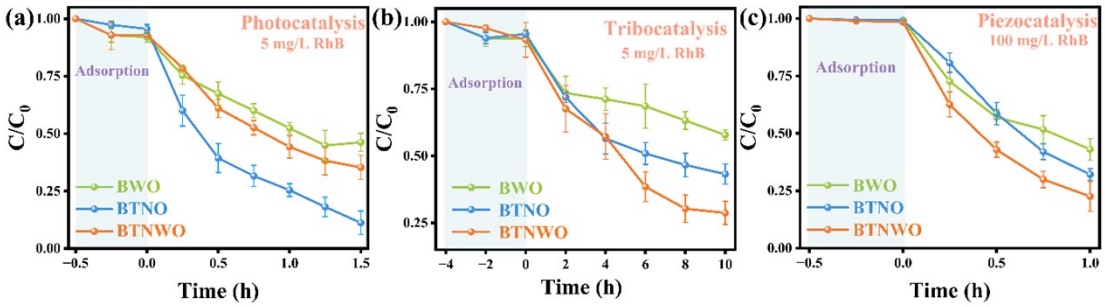

Fig. S20. Plots showing the RhB degradation efficiency when using BWO, BTNO, and BTNWO under (a) photocatalytic, (b) tribocatalytic, and (c) piezocatalytic conditions.

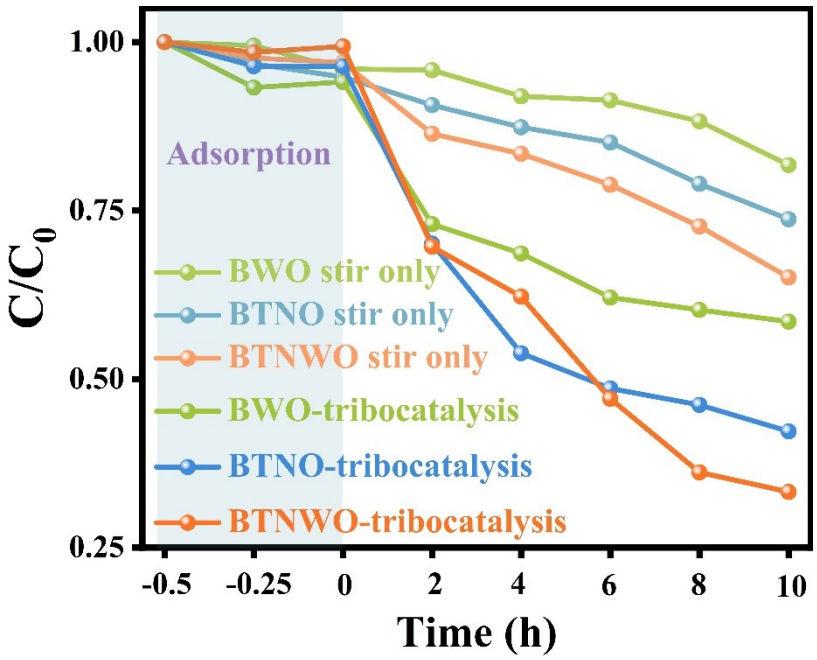

Fig. S21. RhB degradation efficiency by BWO, BTNO, and BTNWO when the stirring paddle (PTFE) is in contact or not in contact with the bottom of the three-necked flask at a rotating speed of 600 rpm.

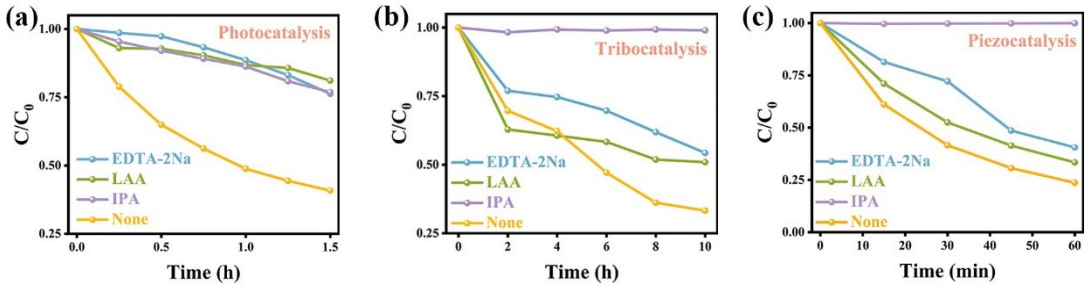

Fig. S22. Time-dependent degradation curves of RhB when using BTNWO with and without the addition of scavengers.

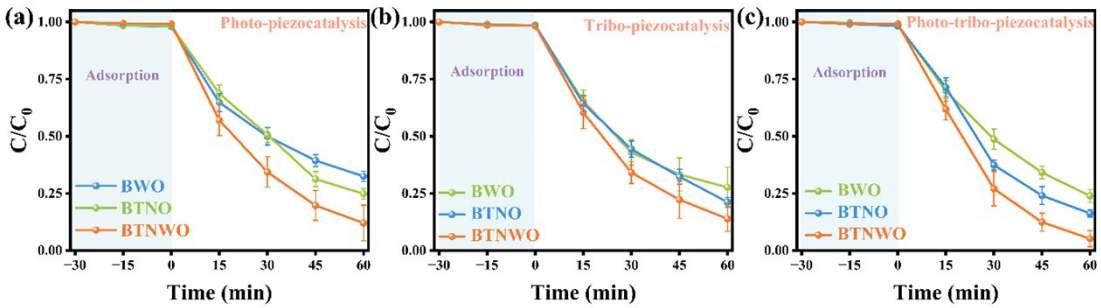

Fig. S23. Plots showing the RhB degradation efficiency of BWO, BTNO, and BTNWO under (a) photo-piezocatalytic, (b) tribo-piezocatalytic, and (c) photo-tribo-piezocatalytic conditions.

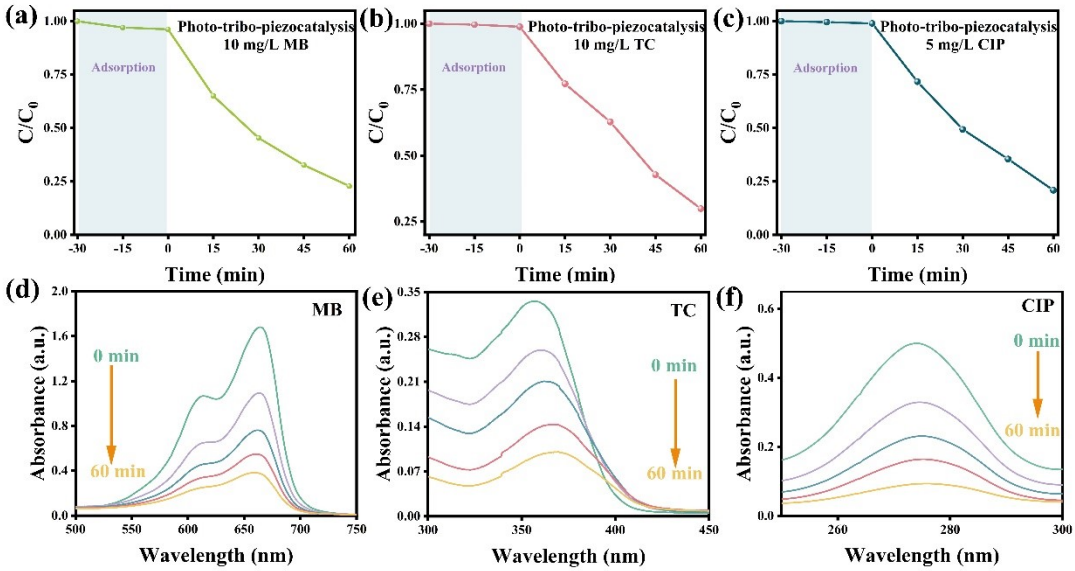

Fig. S24. Degradation efficiencies of (a) MB, (b) TC, and (c) CIP during photo-tribo-piezocatalytic reaction, and (d-f) the corresponding time-resolved UV-vis absorption spectra of BTNWO.

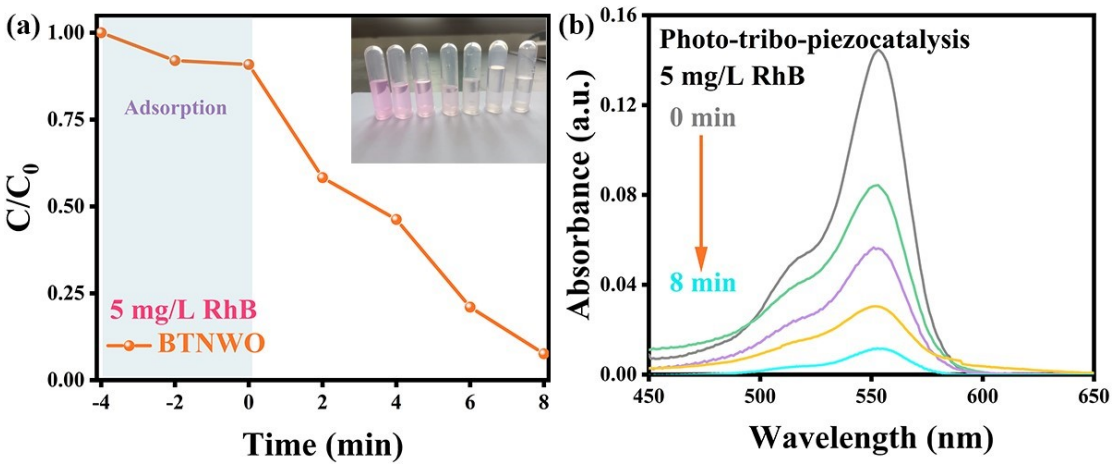

Fig. S25. (a) Photo-tribo-piezocatalytic degradation efficiency of RhB (5 mg/L) when using BTNWO as a catalyst and (b) the corresponding time-dependent UV-vis absorption spectra.

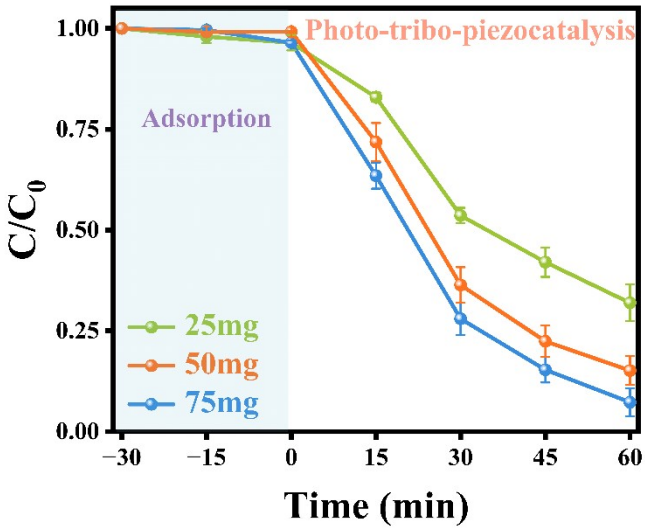

Fig. S26. Photo-tribo-piezocatalytic degradation efficiency of RhB when using BTNWO at different catalyst dosages.

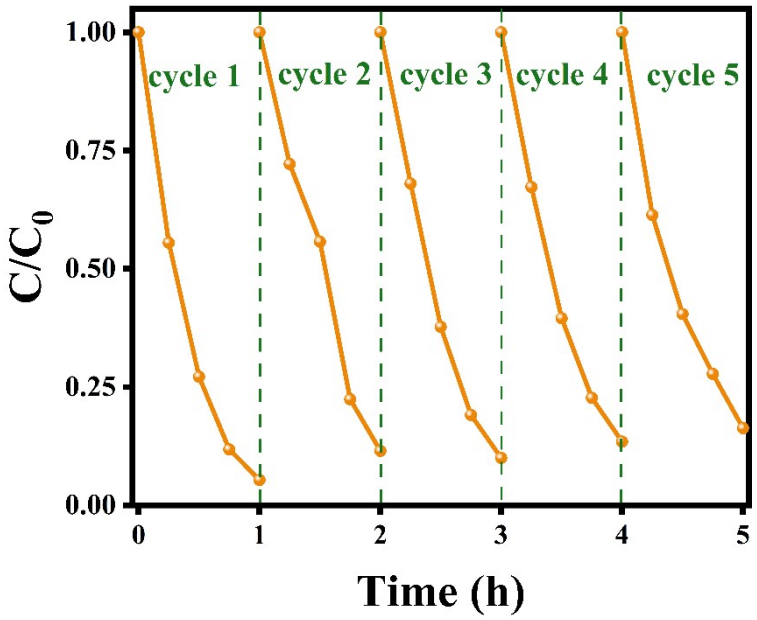

Fig. S27. Cycling tests of photo-tribo-piezocatalytic RhB degradation using BTNWO.

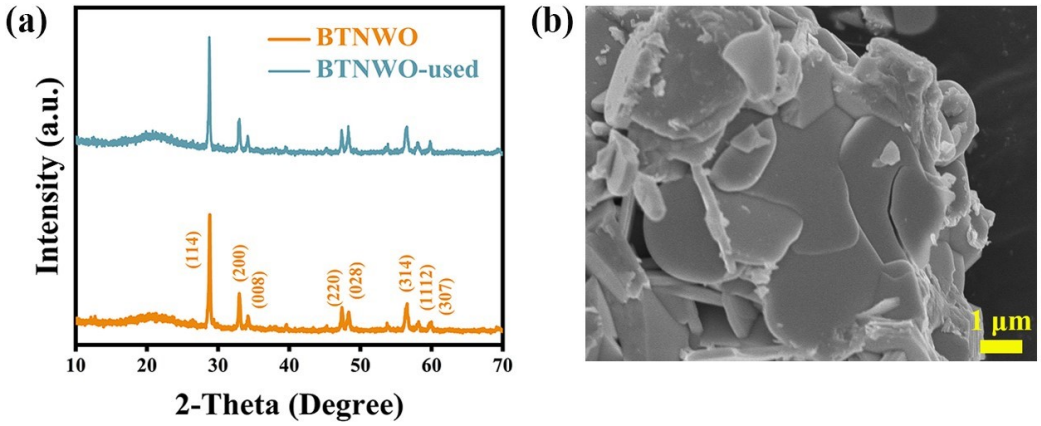

Fig. S28. (a) XRD patterns and (b) SEM image of BTNWO after five consecutive catalytic experiments.

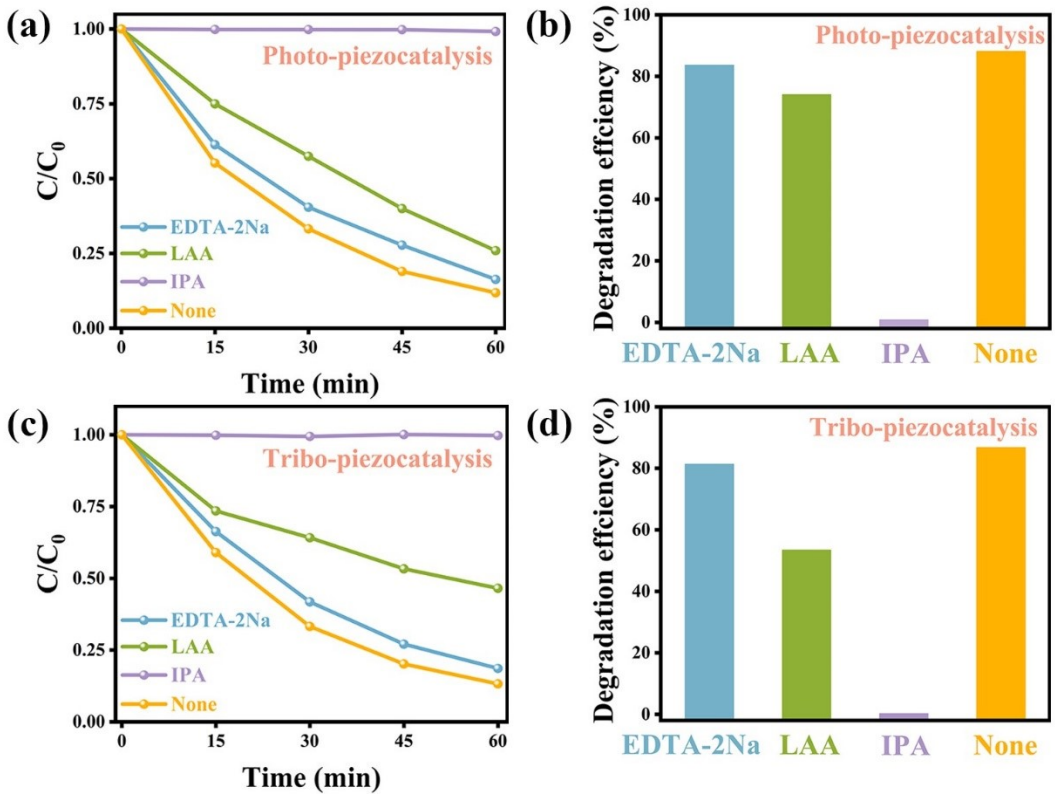

Fig. S29. Time-dependent degradation curves of RhB when using BTNWO with and without the addition of scavengers under (a) photo-piezocatalytic and (b) tribo-piezocatalytic conditions. Corresponding RhB degradation efficiency observed at t = 60 min when under (b) photo-piezocatalytic and (d) tribo-piezocatalytic conditions.

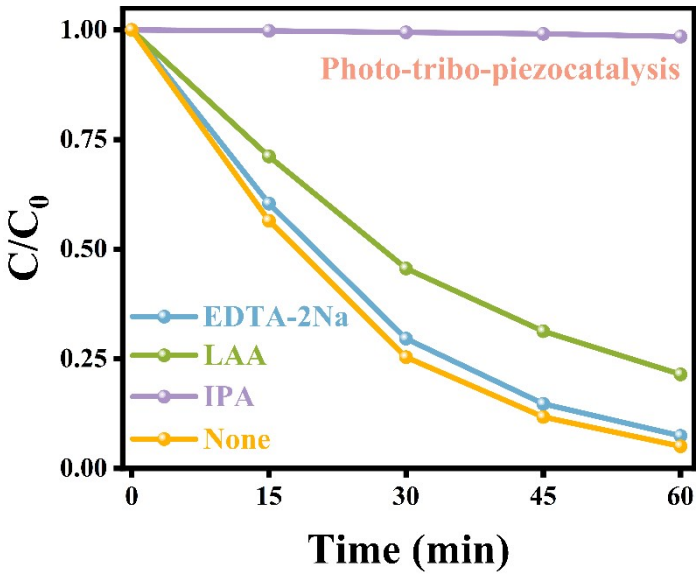

Fig. S30. RhB degradation activity of BTNWO with and without scavengers.

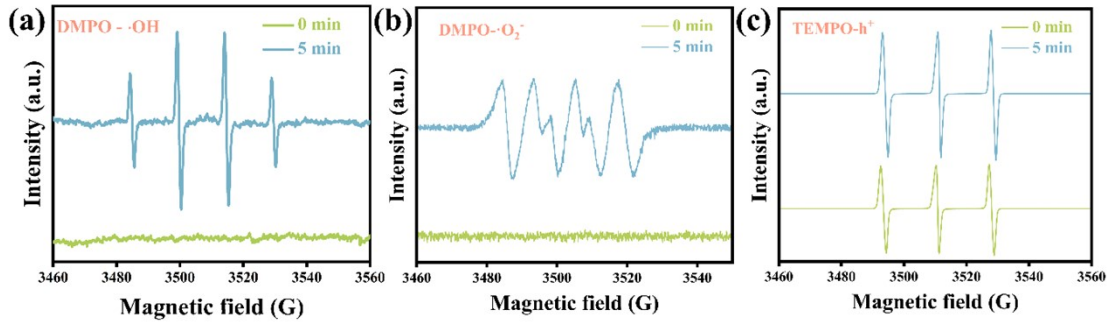

Fig S31. (a - c) ESR spin-trapping to identify the formation of •OH, $•O_2^-$ and h^+ radicals, respectively, by BTNWO.

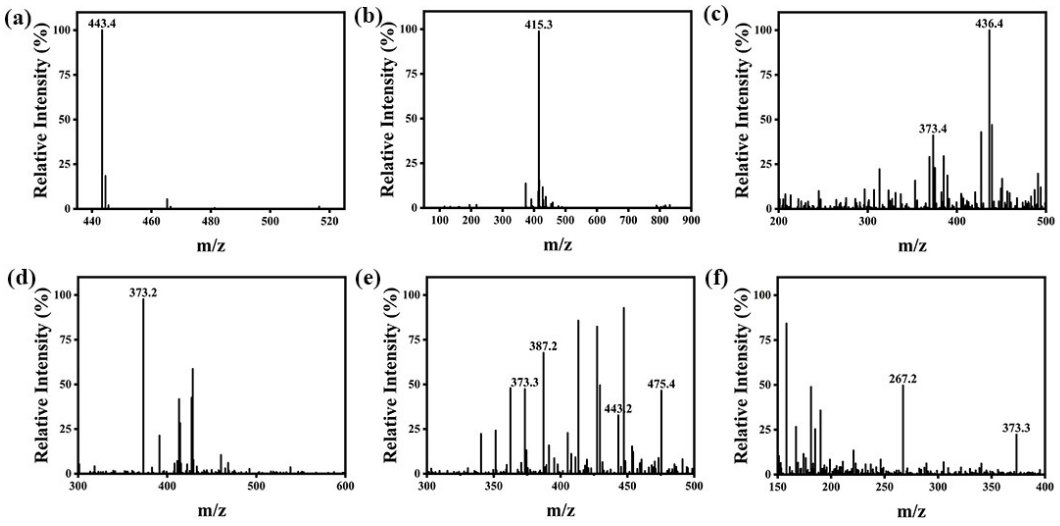

Fig. S32. (a - f) Mass charge spectra of RhB degradation products during photo-tribo-piezocatalysis using BTNWO.

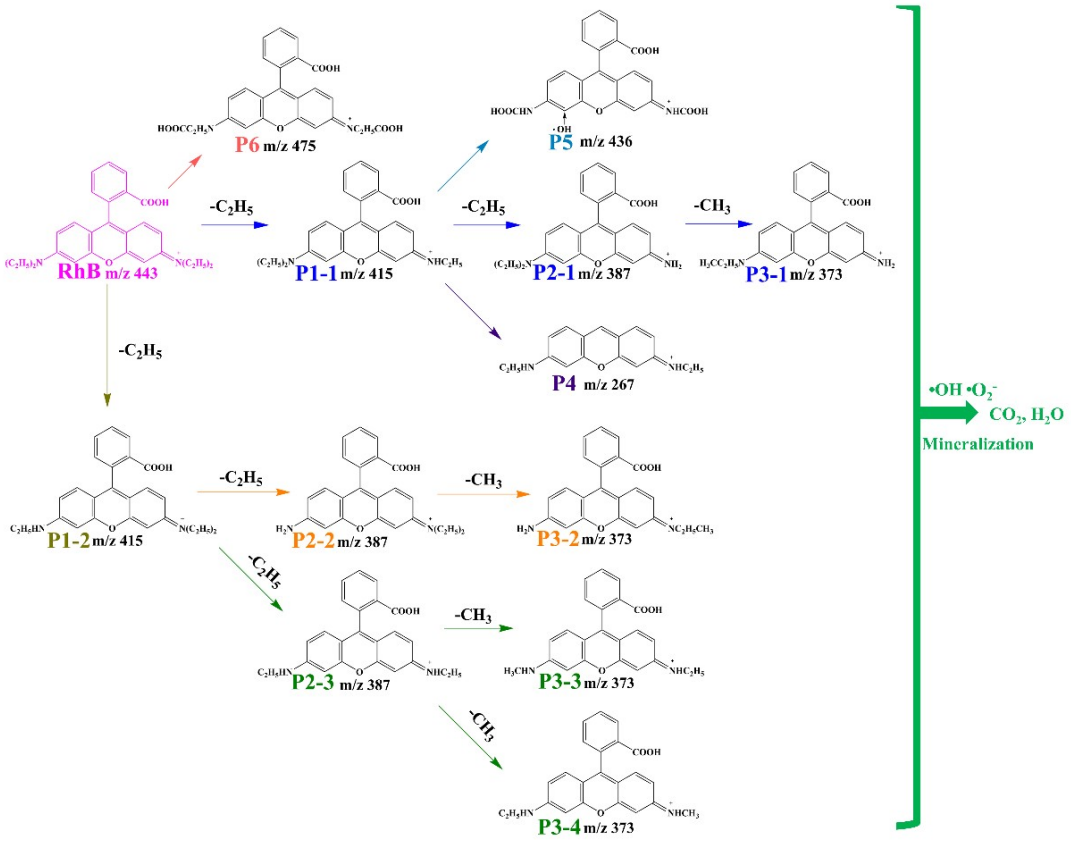

Fig. S33. Proposed pathways for RhB degradation when using BTNWO as a catalyst.

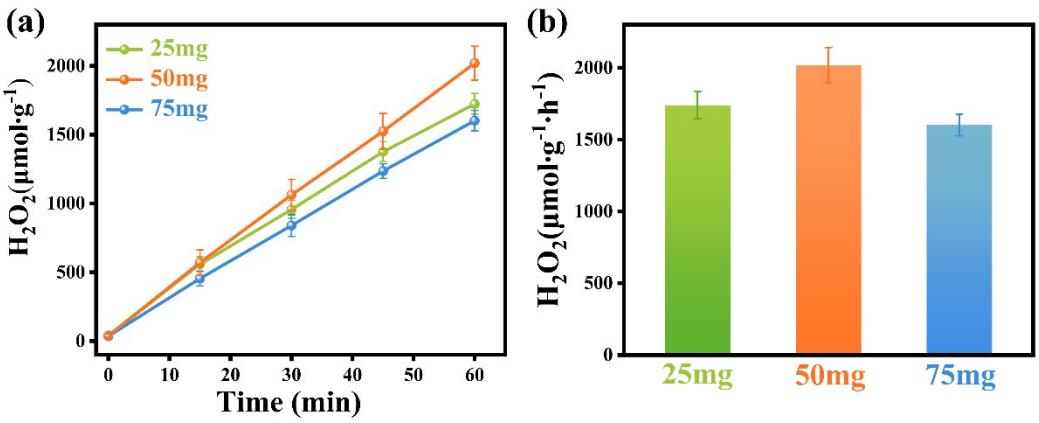

Fig. S34. (a) Photo-tribo-piezocatalytic H_2O_2 production yield and (b) corresponding H_2O_2 production rates of BTNWO with different catalyst dosages.

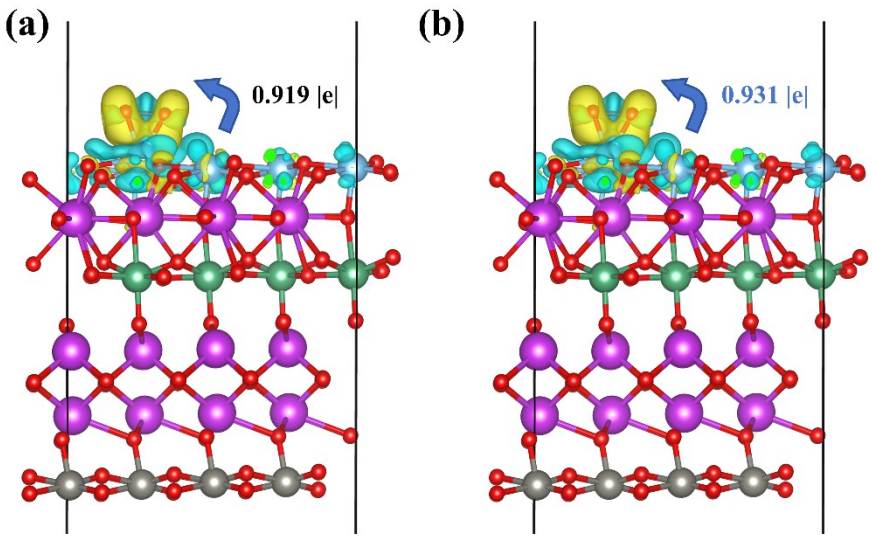

Fig. S35. Charge density difference of O_2 adsorbed on BTNWO (a) without stress and (b) under stress.

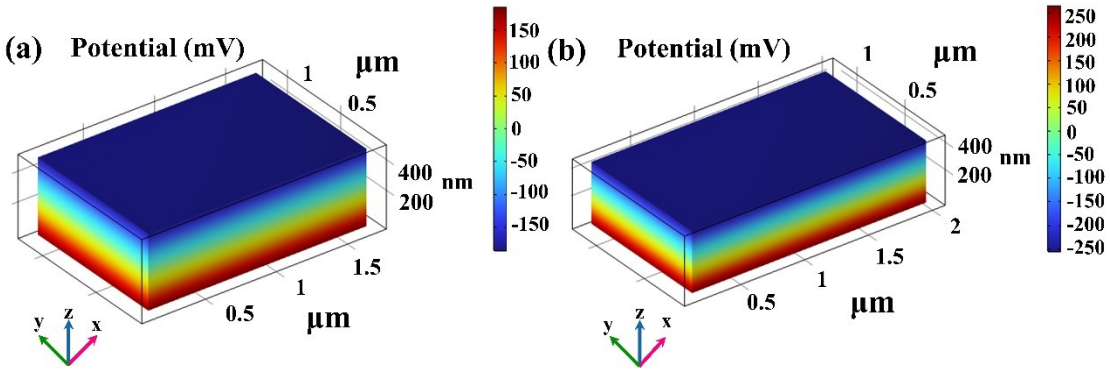

Fig. S36. COMSOL simulation analysis of piezoelectric potential distribution in (a) BWO and (b) BTNO models.

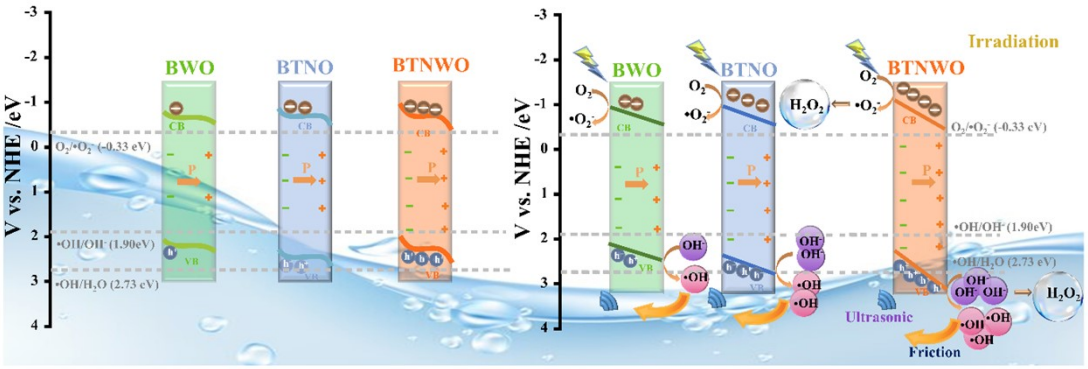

Fig. S37. Schematic illustration for energy band structures and the proposed reaction mechanism of all samples with and without synergetic excitation of irradiation, friction stirring, and ultrasonic vibration.

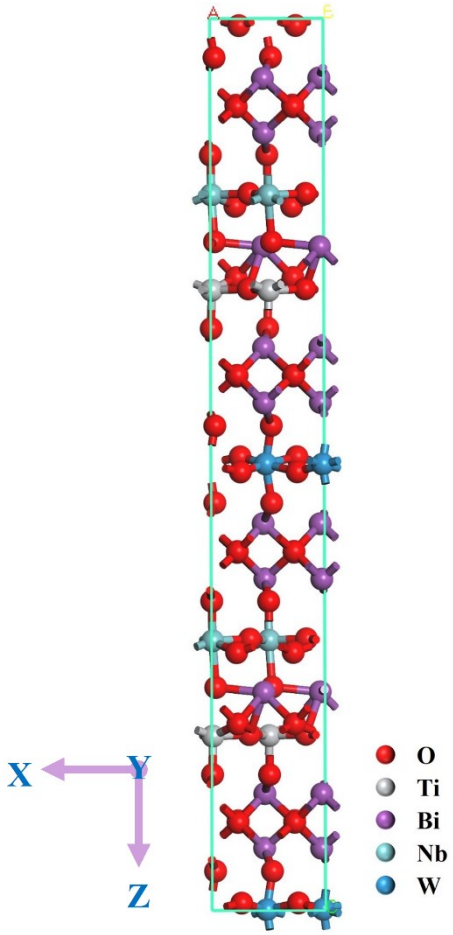

Fig. S38. Schematic diagram of BTNWO bulk phase structure.

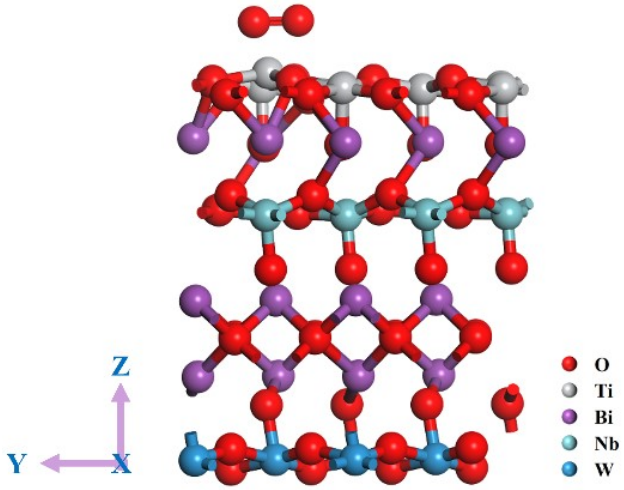

Fig. S39.The model used for simulating O_2 adsorption on the BTNWO (Ti as the active site).

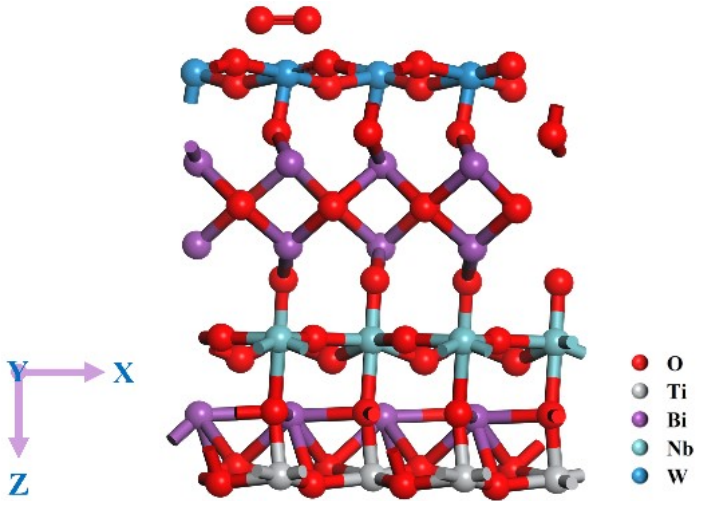

Fig. S40.The model used for simulating O_2 adsorption on the BTNWO (W as the active site).

3. Supplementary Tables

Table S1. Comparison of RhB degradation performance in this work with other reported designs.

Catalyst	Catalyst Concentration (mg/L)	RhB Concentration (mg/L)	Condition	$k\times10^{-3}$ (min^{-1})	Ref
$Bi_5TiNbWO_{15}$	**500**	**100**	**Ultrasonic: 40 kHz, 240 W Light: 300 W Xe lamp (100mW cm^{-2})**	**48.2**	**This work**
$Bi_5TiNbWO_{15}$	**500**	**100**	**Mechanical stirrer: 80 W Ultrasonic: 40 kHz, 240 W Mechanical stirrer: 80 W**	**25.7**	**This work**
$NaNbO_3/CuBi_2O_4$	1000	10	Ultrasonic: 40 kHz 35 W Light: 50 W	11.2	7
$BaZr_{0.02}Ti_{0.98}O_3$	10000	6	Ultrasonic: 40 kHz, 80 W Light: 300 W Xe lamp	8.80	8
$NaNbO_3/WO_3$	250	10	Ultrasonic: 40 kHz, 300 W Light: 300 W UV light	10.7	9
CAU-17	1000	5	Ultrasonic: 40 kHz, 100 W	39	10
SnS_2	300	20	Ultrasonic: 40 kHz, 120 W	12	11
$PbBiO_2I$	1000	10	Ultrasonic: 40 kHz, 120 W	2.4	12
ZnO hollow pitchfork	1000	10	Ultrasonic: 40 kHz, 300 W	8.90	13
$CuBi_2O_4$	500	5	Ultrasonic: 40 kHz, 120 W,	16.2	14
β-$BaTi_2O_5$	1000	10	Ultrasonic: 40 kHz, 300 W,	3.7	15
$BaTiO_3/SrTiO_3$	1000	1	Ultrasonic: 40 kHz, 300 W Light: 300 W UV light	3.1	16
$CNT/Bi_4O_5I_2$	1000	5	Ultrasonic: 40 kHz, 80 W	15	17
$Bi_2S_3/PbBiO_2Cl$	1000	5	Ultrasonic: 40 kHz, 60 W	32.5	18
DR-MoS_2	100	10	Ultrasonic: 40 kHz, 150 W	1.597	19
6H-SiC NPs	1000	5	Ultrasonic: 120 W	0.957	20
$Fe_2O_3/BiVO_4$	1000	4.79	Light: 500 W Xe lamp	1.3	21
Au-ZnO	1000	4.79	Light: 300 W Xe lamp	138.6	22

Ag doped TiO_2	1000	100	Light: 125 W Hg lamp	161	23
Ag on ZnO	400	110	Light: 40 W Xe lamp	30.56	24
TPP/AgBr	500	10	Light: 300 W Xe lamp	59.61	25
BiOBr/BNQDs	600	20	Light: 300 W Xe lamp	69.6	26
Ag-Ce/ZnO	250	10	Light: 300 W Xe lamp	98.8	27
NiO/RGO	200	10	Light: 30 W Xe lamp	15.871	28
$ZnO/CuWO_4$	140	0.479	Light: 150 W lamp	7.86	29
BiOBr/ZIF-67	1000	20.0	Light: 400 W Xe lamp	23.2	30
$BiVO_4$	1000	4.22	Light: 300 W Xe lamp	1.3	31
Bi_4TaO_8Cl	1600	9.58	Ultrasonic: 37/80 kHz 110 W Light: 400 W	269.4	32

Table S2. Comparison of H_2O_2 generation performance in this work with other reported designs.

Catalyst	Catalyst Concentration (mg/L)	Condition	H_2O_2 ($\mu mol \cdot g^{-1} \cdot h^{-1}$)	Ref
$Bi_5TiNbWO_{15}$	**1000**	**Ultrasonic: 40 kHz, 240 W Light: 300 W Xe lamp (100mW cm^{-2}) Mechanical stirrer: 80 W**	**1996**	**This work**
ZC50	500	Ultrasonic: 25/40 kHz 480 W Light: 300 W Xe lamp	1450	33
Mo_5Fe_5	2500	Ultrasonic: 40 kHz 120 W Light: 24 W Xe lamp Sacrificial Agent: C_2H_5OH	142	34
$Bi_4W_{0.5}Ti_{0.5}O_8Cl$	500	Ultrasonic: 40 kHz 300 W Light: 300 W Xe lamp	530	35
$BaTiO_3$:Nb/C	500	Ultrasonic: 40 kHz 150 W Light: 300 W Xe lamp Sacrificial Agent: C_2H_5OH	1360	36
SP-CN	1000	Ultrasonic: 40 kHz 300 W Light: 300 W Xe lamp	76	37
$C_{0.02}$-ZnO	500	Ultrasonic: 45 kHz 200 W	588	38
NFO–N_2	625	Ultrasonic: 40 kHz 150 W	456	39
BCZT-0.5	300	Ultrasonic: 40 kHz 180 W Sacrificial Agent: C_2H_5OH	433	40
UBTO-OV2	500	Ultrasonic: 40 kHz 300 W Sacrificial Agent: C_2H_5OH	1611	41
Bi_3TiNbO_9	1000	Ultrasonic: 40 kHz 50 W	407	42
Ti_3SiC_2	20	Ultrasonic: 40 kHz 180 W Sacrificial Agent: C_2H_5OH	871	43

10%Co-BiOBr	250	Ultrasonic: 40 kHz 300 W	381	44
$Bi_4O_5Br_2$	200	Ultrasonic: 40 kHz 300 W	2700	45
Hf-UiO-66	20	Ultrasonic: 40 kHz 300 W Sacrificial Agent: C_2H_5OH	1131	46
$Bi_4O_5Br_2$/g-C_3N_4	1000	Light: 300 W Xe lamp	124	47
ZIS/BTO-2	667	Light: 300 W Xe lamp Sacrificial Agent: C_2H_5OH	827	48
Bi/BiOCl-2	1250	Light: 300 W Xe lamp 5 vol% HCOOH	4320	49
IrO_2-Pt/Bi_2YO_4Cl	1000	Light: 300 W Xe lamp	647	50
Au/Bi_2O_3-TiO_2	2000	Light: 300 W Xe lamp Sacrificial Agent: C_2H_5OH	467	51
$Bi_{3.6}K_3$-CN	300	Light: 300 W Xe lamp Sacrificial Agent:C_2H_5OH	1341	52
Au/F-TiO_2	2000	Light: 300 W Xe lamp Sacrificial Agent: C_2H_5OH	167	53
Pd/PEI/BOC	1000	Light: 300 W Xe lamp 5 vol% HCOOH	3700	54
g-C_3N_4	2000	Light: 350 W Xe lamp Sacrificial Agent: C_3H_8O	1125	55
CoP-C_3N_4	1000	Light: 300 W Xe lamp	22	56
$BiVO_4$	1000	Light: LED lamp (50 mW cm^{-2})	35.71	57
BiOBr	150	Ultrasonic: 37 kHz, 110 W	2700	58
$BiVO_4$	400	Ultrasonic: 40 kHz, 100 W	151	59
PCCN	2500	Ultrasonic: 100 W Light: 300 W Xe lamp Sacrificial Agent: C_2H_5OH	4613	60
Ag/g-CN	100	Ultrasonic: 70 W Light: 120 W Xe lamp	3964	61
$Sr_2Bi_3Ta_2O_{11}Cl$	200	Light: 400 W Xe lamp	2960	62

References

1. G. Kresse, and J. Furthmüller, *Phys. Rev. B* 1996, **54**, 11169-11186.

2. H. S.Taylor and E. F. Armstrong, *Proc. R. Soc*. 1925, **108**, 105-111.

3. J. P. Perdew, K. Burke and M. Ernzerhof, *Phys. Rev. Lett*. 1996, **77**, 3865-3868.

4. G. Kresse and D. Joubert, *Phys. Rev. B* 1999, **59**, 1758-1775.

5. J. Klimeš, D. R. Bowler and A. Michaelides, *Phys. Rev. B* 2011, **83**, 195131.

6. S. Grimme, J. Antony, S. Ehrlich and H. Krieg, *J. Chem. Phys*. 2010, **132**, 154104.

7. K. D. Rajan, P. P. Gotipamul, S. Khanna, S. Chidambaram, M. Rathinam, Materials Letters, 2021, **296**, 129902.

8. M. Sharma, G. Singh and R. Vaish, *J. Am. Ceram. Soc*, 2020, **103**, 4774-4784.

9. X. Yan, S. Zhang, L. F. Pan, T. Ai, Z. Li, Y. H. Niu, *Inorganic Chemistry Communications*, 2023, **158**, 111510.

10. S. H. Dong, L. Y. Wang, W. Y. Lou, Y. X. Shi, Z. Z. Cao, Y. F. Zhang, J. M. Sun, *Ultrasonics Sonochemistry*, 2022, **91**, 106223.

11. R. R. Jiang, G. H. Lu, M. Wang, Y. F. Chen, J. C. Liu, Z. H. Yan and H. J. Xie, *NPJ Clean Water* 2023, **6**, 1-12.

12. Z. Y. Li, Q. L. Zhang, L. K. Wang, J. Y. Yang, Y. Wu and Y. M. He, *Ultrason. Sonochem*. 2021, **78**, 105729.

13. A. Sharma, U. Bhardwaj and H. S. Kushwaha, *Catal. Sci. Technol*, 2022, **12**, 812-822.

14. Y. F.Cao, T. F. He, M. J. Li, Z. Z. Cao, Y. F. Gao, J. R. Liu and G. R. Li, *J. Phys. Chem. Solids*, 2022, **167**, 110732.

15. X. Li, H. J. Zheng, J. J. Liu, H. C. Li, J. Wang, K. Yan, J. S. Liu, F. Dang and K. J.

Zhu, *Mater. Technol*, 2023, **38**, 2163474.

16. X. T. Liu, X. F. Shen, B. S. Sa, Y. G. Zhang, X. Li and H. Xue, *Nano Energy*, 2021, **89**, 106391.

17. Y. Wang, D. F. Yu, Y. Liu, X. Liu and Y. Shi, *Materials*, 2021, **14**, 4449.

18. Y. K. Zheng, Y. X. Chu, R. Y. Dong, J. T. Xu, L. H. Zhao, K. Q. Wang, Y. Wu, Y. M. He, *Journal of Alloys and Compounds*, 2025, **1037**, 182237.

19. S. H. Li, X. E. Ning, P. Y. Hao, Y. L. Cao, J. Xie, J. D. Hu, Z. J. Lu, A. Z. Hao, *Dyes and Pigments*, 2022, **206**, 110678.

20. L. L. Zhou, T. Yang, K. Wang, L. P. Zhu, E. H. Wang, K. C. Chou, H. L. Wang, X. M. Hou, *Rare Met*, 2024, **43**, 3173–3184.

21. P. Cai, S. M. Zhou, D. K. Ma, S. N. Liu, W. Chen, S. M. Huang, *Nano-Micro Lett*, 2015, **7**, 183-193.

22. M. lrfan, A. A. Haidri, B. Ahmad, W. Mnif, l. Kebaili, M. l. Khan, M, *Opt. Mater,* 2024. **154**. 115681.

23. V. Soni, A. N. Singh, P. Singh, A. Gupta, *RSc Adv*. 2022.**12**,18794-18805.

24. T. A. Alrebdi, R. A. Rezk, S. M. Alghamdi, H. A. Ahmed, F. H. Alkallas, R. A. Pashameah, A. M.Mostafa, E. A. Mwafy, *Membranes*, 2022. **12**. 877.

25. Z. Song, H. Ma, J. Lu, G. Huang, Q. Gao, C. Xiao, *ChemistrySelect*, 2025, **33**, 03075.

26. Y. Qin; X. Peng, T. Wu, Y. Zhong, H. Xu, Z. Mao, L. Zhang, *Catalysts*, 2025, **15**, 771.

27. R. J. Liu, X. N. Fu, Y. F. Guo, J. F. Zhang, W. F. Tian, *Vacuum*, 2023, **215**, 112337.

28. P. Vivek, R. Sivakumar, E. S. Esakki, S. Deivanayaki, *Journal of Physics and Chemistry of Solids*, 2023, **176**, 111255.

29. J. P. C. Moura, R. Y. N. Reis, A. E. B. Lima, R. S. Santos, G. E. Luz, *Journal of Photochemistry and Photobiology A: Chemistry*, 2020, **401**, 112778.

30. R. Q. Zhong, H. W. Liao, Q. L. Deng, X. H. Zou, L. X. Wu, *Journal of Molecular Structure*, 2022, **1259**, 132768.

31. P. Cai, S. M. Zhou, D. K. Ma, S. N. Liu, W. Chen, S. M. Huang, *Nano-Micro Lett*, 2015, **7**, 183-193.

32. M. Banoo, J. Kaur, A. K. Sah, R. S. Roy, M. Bhakar, B. Kommula, G. Sheet and U. K. Gautam, *ACS Appl. Mater. Interfacecs*. 2023, **15 (27),** 32425-32435.

33. L. H. Meng, C. Zhao, X. Zhang, R. X. Guo, Y. F. Zheng, H. Y. Chu, H. F. Fu, P Wang, C. C. Wang, *Nano Energy*, **2024**, 128, 109795.

34. Y. R. Lu, Y. B. Dong, W. Liu, Q. Jin, H. Lin, Chemical Engineering Journal, 2025, **508,** 160935

35. S. C. Tu, Y. Q. Wang, H. W. Huang, J. J. Zhang, H. Li, J. C. Sun, T. Chen, Y. H. Zhang, *Chemical Engineering Journal*, 2023, **465**, 142777.

36. X. Zhou, F. Yan, A. Lyubartsev, B. Shen, J. Zhai, J. C. Conesa, N. Hedin, *Advanced Science*, 2022, **9**, e2105792.

37. Z. Guo, K. Sun, S. Zou, B. Xiong, L. Wang, W. Shi, Y. Sun, F. Guo, *Colloid Interface Sci*, 2025, **699**, 138118.

38. Y. Wen, W. Liu, P. Wang, *Adv. Funct. Mater*, 2023, **33**, 2308084.

39. N. Wang, R. X. Wang, Z. J. Li, R. Liu, H. Gao, H. Y. Chen, R. Li, Y. Z. Long, H. D. Zhang, *ACS Applied Nano Materials*, 2023, **6**, 15063-15072.

40. K. Wang, M. Q. Zhang, D. G. Li, *Nano Energy*, 2022, **98**, 107251.

41. C. Y. Wang, F. Chen, C. He, *Chem. Eng. J.*, 2022, **431**, 133930.

42. Y. F. Cui, F. Wang, P. Yuan, *ACS Sustain. Chem. Eng.*, 2024, **12**, 3595-3607.

43. Y. Jia, K. Wang, C. Li, *Mater. Today Sustain.*, 2023, **22**, 100390.

44. A. Hao, Y. L. Ye, Y. G. Ran, J. Y. Zhu, S. S. Hu, X. R. Zeng, X. N. Liu, *Langmuir Article ASAP*.

45. H. Cai, F. Chen, C. Hu, *Chin. J. Catal.*, 2024, **57**, 123-132.

46. W. Yuan, H. Yao, J. Zhang, *Asia-Pac. J. Chem. Eng.*, 2025, **20**, e70013.

47. X. S. Zhao, Y. Y. You, S. B. Huang, *Appl. Catal. B Environ.*, 2020, **278**, 119251.

48. H. Fan, L. Ai, M. Xu, *J. Colloid Interface Sci.*, 2025, **697**, 137896.

49. L. R. Liu, H. P. Fu, Y. T. Zeng, L. Feng, T. X. Zhang, Q. S. Liang, X. F. Xiao, *New J. Chem.*, 2022, **46**, 22419-22426.

50. S. M. Li, Y. Xu, K. Liang, X. W. Qu, Z. C. Feng, Y. Qi, B. B. Dong, *J. Energy Chem.*, 2025, **111**, 79-85.

51 L. W. Feng, B. D. Li, Y. Q. Xiao, L. J. Li, Y. Q. Zhang, Q. N. Zhao, G. F. Zuo, X. G. Meng, V. A. L. Roy, *Catalysis Communications*, 2021, **155**, 106315.

52. H. Liang, A. Wang, R. Cheng, *Chem. Eng. J.*, 2024, **489**, 151145.

53. L. J. Li, B. D. Li, L. W. Feng, X. Q. Zhang, Y. Q. Zhang, Q. N. Zhao, G. F. Zuo, X. G. Meng, *Molecules*, **2**021, **26**, 3844.

54. M. Zhang, X. Li, Y. Liu, W. Wang, Y. Zhang, *New J. Chem*., 2024, **48**, 11794-11801.

55. L. Hu, M. Y. Du, R. Liu, *J. Colloid Interface Sci.*, 2025, **679**, 456-464.

56. J. Kaito, M. Watanabe, R. Miyoshi, T. Kamegawa, K. Mori, H. Yamashita, *Catal. Today*, 2024, **426**, 114400.

57. Y. Li, Z. Q. Liu, W. J. Qi, H. Y. Shi, K. Y. Wang, X. F. Wang, P. Wang, F. Chen, H. G. Yu, *Appl. Surf. Sci*, 2024, **656**, 159664.

58. M. Banoo, K. Samanta, A. K. Sah, R. S. Roy, M. Bharkar, D. Sanyal, D. G. Porob, K. Glazyrin, D. Topwal, G. Sheet, D. Ghosh, and U. K. Gautam, *Adv. Funct. Mater.* 2024, **34(49),** 2411464.

59. T. F. Cui, H. R. Yang, W. Z. Zhou, S. Pal, J. Briscoe, G. D. Shen, X. M. Tao, *Colloid Interface Sci*, 2025, **703**, 139211.

60. Z. Chen, D. Yan, X. Wang, G. Ding, Z. Wang, Y. Xiao, X. Liu, P. Wang, L. Chen, L. Shuai, G. Liao, *ACS Catal*., 2025, **15**, 13568-13580.

61. H. P. Nguyen, H. N. M. Quang, H. C. Kung, L. T. N. Huynh, T. L. Nguyen, S. J. You, B. W. Huang, M. T. P, G. P. Chang-Chien, *Optical Materials*, **2025**, 168, 117423.

62. M. Banoo, A. K. Sah, R. S. Roy, K. Kaur, B. Kommula, D. Sanyal, and U. K. Gautam, *Chem. Sci*., 2024, **15**, 17049-17057.